

**AN FPGA-BASED MICROARCHITECTURE FOR THE
IMPLEMENTATION OF QUANTUM GATES WITH
TRAPPED IONS**

A Thesis
Presented to
The Academic Faculty

by

C. Spencer Nichols

In Partial Fulfillment
of the Requirements for the
Undergraduate Thesis for the
School of Physics

Georgia Institute of Technology
December 2012

**AN FPGA-BASED MICROARCHITECTURE FOR THE
IMPLEMENTATION OF QUANTUM GATES WITH
TRAPPED IONS**

Approved by:

Professor Kenneth Brown, Advisor
School of Chemistry and Biochemistry
Georgia Institute of Technology

Professor T. A. B. Kennedy
School of Physics
Georgia Institute of Technology

Date Approved: 15 December 2012

To everyone who made this possible.

ACKNOWLEDGEMENTS

I want to thank Dr. Brown for giving me the opportunities to pursue and expand my career in experimental physics.

TABLE OF CONTENTS

DEDICATION	iii
ACKNOWLEDGEMENTS	iv
LIST OF FIGURES	vii
I INTRODUCTION	1
II QUANTUM COMPUTING WITH TRAPPED IONS	2
III LINEAR ION TRAPS	7
3.1 Introduction to Ion Traps	7
3.2 The Mathieu Equation	7
3.3 Trap Stability	9
3.4 Secular Frequency and Micromotion	10
3.5 Loading $^{40}\text{Ca}^+$	13
IV CALCIUM ION QUBITS	14
4.1 The Electronic Structure of $^{40}\text{Ca}^+$	14
4.2 Doppler Cooling	15
4.3 Qubits and Rabi Transitions	18
4.4 Sideband Cooling	21
V CONTROL INTERFACE	24
5.1 Acousto-Optic Modulators	24
5.2 Direct Digital Synthesizers	27
5.3 FPGA Microarchitecture	29
VI $^{40}\text{Ca}^+$ SPECTROSCOPY	32
6.1 AOM Power Scan	32
6.2 $^{40}\text{Ca}^+$ 397 nm and 729 nm Transition Spectroscopy	32
VII CONCLUSION	35

APPENDIX A — RELATIONS BETWEEN A AND Q IN THE MATHIEU EQUATION TO THE SECOND ORDER	36
REFERENCES	37

LIST OF FIGURES

1	Linear Paul Trap and Fields	8
2	Mathieu Stability Chart	10
3	Calcium Ionization Transition and Ion Trap Setup	13
4	Calcium Qubit Energy Levels	15
5	Doppler Cooling	16
6	729 nm Transition Sideband Cooling	23
7	Acousto-Optic Modulator Diagram and Setup	25
8	Complete Laser Control Setup	25
9	Bragg Condition Inside an Acousto-Optic Modulator	26
10	Direct Digital Synthesizer Diagram	28
11	FPGA Internal Architecture	30
12	AOM Power Scan	33
13	397 nm and 729 nm Transition Spectroscopy Data	34

CHAPTER I

INTRODUCTION

The field of quantum computing has grown significantly in the past 30 years from initial theory to experimental implementations of quantum gates in a variety of media. Currently, trapped ions are an ideal medium for implementing quantum gates since they can be used to create gates with very high fidelities and store information with long coherence times [1]. Implementing an ion-based quantum computing architecture requires the creation of many coherent laser pulses of precise frequency with relative phase control as well as the application of voltages to the ion trap itself. Most importantly, both laser pulses and trap voltages must be applied with very precise timing in order to maximize gate fidelity. The need for such exacting control of many diverse instruments requires a controlling infrastructure that is general enough to adapt to the needs of an arbitrary experiment while maintaining very precise timing. Using the flexibility of FPGAs, I have created a microarchitecture that combines a single general microprocessor and a timing-specific bank of parallel processors that control digital to analog converters (DACs), direct digital synthesizers (DDSs) analog to digital converters (ADCs), and general digital communication channels for shaping specific laser pulses and the general control existing equipment. The microarchitecture was then tested by performing basic spectroscopy on calcium ions. This demonstrates its ability to create basic laser pulse sequences that will be necessary for implementing quantum gates in the future.

CHAPTER II

QUANTUM COMPUTING WITH TRAPPED IONS

Quantum bits (qubits) are the quantum mechanical analog to bits in a classical computer. Instead of only storing information in distinct 0 or 1 states, qubits store information in quantum mechanical wavefunctions that can exist as superpositions of the 0 and 1 states. I will expand on the exact working principles of trapped-ion qubits later, but for now, the existence of qubits will be taken as a given so that we can understand the theoretical and experimental difficulties with creating quantum circuits and working with trapped ions. The first problem with creating a quantum computer is that not all n -quantum bit operators are easy to construct, so they must first be decomposed into smaller, more experimentally realizable operations. Also, physically implementing quantum circuits with trapped ions is extremely difficult. Fortunately, experimental research on trapped ion control and manipulation has overcome many of these difficulties, and trapped-ion architectures are now at the forefront of quantum computing research and promise to remain contenders into the near future [1].

Theoretical quantum gate analysis originated from classical studies of reversible Turing machines in the 1960s by Landauer, Fredkin, and Toffoli [2, 3, 4]. Early work by Feynman in the 1980s was followed by explosive growth in the 1990s fueled by Peter Shors discovery that the RSA cryptosystem could be broken by quantum computers [1, 5]. One of the first papers to fully consolidate prior quantum circuit theories into one reference was the work of Barenco *et al.* in 1995 [6]. Their work is primarily focused on the decomposition and special properties of single- and multiple-qubit-controlled gates. For any controlled single qubit gate W , the operation can be broken up into three single-qubit rotations on the target qubit separated by controlled-not

(CNOT) gates between the two qubits [6]. Since single-qubit rotations and CNOT gates are easier to implement, this observation has proved useful by easing the experimental implementation of arbitrary quantum gates. It has also been shown that this proof can be expanded to three-qubit, controlled gates; however, the specific decomposition is very different. All of the rotations of the target qubit are controlled by the states of the control qubits, and the CNOT gates only operate on the controlling qubits [6]. By generalizing their proofs on two- and three-qubit gate decomposition to arbitrary n-qubit gates, Barenco *et al.* lay the framework for continued research into arbitrary quantum gate simulation from one- and two-qubit gates.

Expanding on the work of Barenco *et al.*, many have tried to further decompose arbitrary n-qubit operators for better experimental implementation. In 2004, Vidal and Dawson found a complete decomposition of arbitrary two-qubit gates [7]. Unlike the controlled rotations in Barenco *et al.*, Vidal and Dawson show that any arbitrary two-qubit gates that simultaneously act on both qubits can be transformed into three pairs of single-qubit rotations separated by CNOT gates, and they proceed to show special cases that can be further decomposed [7]. In contrast to the work of Vidal and Dawson, the work of Shende, Markov, and Bullock does not attempt to decompose quantum gates; instead, their work shows that there are limits to how far gates can be decomposed. If one only uses single-qubit rotations and CNOT gates, almost all n-qubit operators require a circuit with more than $\frac{1}{4}[4n - 3n - 1]$ CNOT gates [8]. Putting lower and upper bounds to the decomposition of arbitrary n-qubit operators into single-qubit rotations and CNOT gates means that one must either deal with the consequences of only using single-qubit rotations and CNOT gates or find more complicated bases to work in. However, building n-qubit gates from CNOT and single-qubit gates has proved invaluable for implementing complex quantum operations.

In these theoretical works, qubits are treated as abstract two-level quantum systems. Here, we will examine trapped ions as a specific physical implementation. Using atomic orbitals of cold, trapped ions for quantum computation was first suggested by Cirac and Zoller in 1994. Focusing on the implementation of an n-qubit CNOT gate, Cirac and Zoller show how motional modes in a linear trap can be used to physically implement a two-qubit gate. For the two-qubit CNOT gate, two atoms are trapped, initialized, and a transition is induced in the control atom via a laser. This transition is accompanied with a momentum kick, and the center-of-mass vibrational mode of both atoms is excited. Finally, a red-detuned laser addresses the target atom to induce a transition, but this transition only occurs if the center-of-mass mode has been excited via the first transition [9]. Along with Sorensen and Molmers later work on ions in thermal motion, Cirac and Zollers theoretical work has been the basis for all experimental research on multi-qubit, trapped-ion, quantum computing [10]. Another key advancement in trapped ion quantum computing has been the creation of an optimized entangling gate. Addressed in the work of Kraus and Cirac, optimal entanglement of Bell states under an arbitrary, two-qubit operator UAB is a function of the eigenvalues of the decomposed operator U_d [11]. With proposed experimental implementations of single-qubit gates and two-qubit entangling gates, theoretical work on quantum computing has been recently transformed into experimental results.

Experimentally realizing quantum computing with trapped ions is very difficult due to the levels of precision necessary to achieve high fidelity quantum circuits. One possible implementation of a quantum computing architecture is demonstrated by Home *et al.* [12]. In their setup, Home describes a series of linear traps in which $^9\text{Be}^+$ computing and storage ions are contained, shuttled, manipulated by laser pulses, and sympathetically cooled with $^{24}\text{Mg}^+$ ions. With a six-region Paul trap, Home *et al.* demonstrate their capabilities by implementing a two-qubit transformation, U, and its square while measuring their fidelities [12]. Optimizing quantum gate fidelities

is achieved by reducing all sources of quantum decoherence, and as discussed in the works of Wineland *et al.* and Turchette *et al.*, there are many different possible sources of decoherence [13, 14]. Wineland and Turchette also discuss decoherence through trap heating due to Johnson noise, patch potentials and oriented domains on the trapping surface, injected noise from controlling electronics, and collisions with background gas. Both groups also provide experimental evidence showing heating rates in different traps due to these sources; however, the work by Wineland *et al.* goes further to show different non-trap related sources of decoherence like frequency and phase instability of acousto-optic-modulators (AOMs)[13]. Remote entanglement is also essential for transferring information between individual quantum processors as described in the work of Olmschenk *et al.* [15]. In this work, they describe a method for remotely entangling $^{171}\text{Yb}^+$ ions using the properties of single photon interactions with a beamsplitter [15]. All of this foundational work has paved the way for recent work on creating scalable quantum computers with trapped ions.

A multi-qubit implementation of a programmable quantum computer has recently been demonstrated by Hanneke *et al.* [16]. Using stimulated-Raman transitions and Rabi oscillations created with laser pulses shaped by AOMs, Hanneke *et al.* describe a programmable, two-qubit quantum computer that can implement any arbitrary two-qubit gate. The programability of their processor is demonstrated by showing the experimental fidelities of 160 different two-qubit operators on all 16 input states; the mean fidelity of all 160 operators is found to be 0.79 [16]. In addition to a fully functioning two-qubit processor, researchers have recently demonstrated five-qubit systems for open quantum system dynamics, three-qubit systems for simulating the Ising model, and the entanglement of 14 qubits [17, 18, 19]. Realizing a programmable, multi-qubit processor has been a triumph for trapped-ion quantum computing research and allows for complex quantum computing architectures.

CHAPTER III

LINEAR ION TRAPS

3.1 Introduction to Ion Traps

Before ions can be used for quantum computing, they must be trapped. Wolfgang Paul invented the first electromagnetic ion traps for mass spectroscopy [20]. Ion traps are still primarily used for mass spectroscopy, but their application has been extended to highly accurate atomic clocks, atomic and molecular spectroscopy, and quantum computing [15, 21, 22, 23]. Earnshaw's theorem states that it is impossible to confine charged particles in three dimensions with electrostatic fields [24]. Instead, linear ion traps, or Paul traps, use radio frequencies to generate oscillating (pondermotive) pseudopotentials capable of trapping charged particles [20]. Linear Paul traps use radio frequency (RF) voltages to create a pseudopotential that only confines ions perpendicular to the primary trap axis. To keep trapped ions from escaping along the trap axis, endcaps with DC voltages create a parabolic potential well that pushes ions towards the center of the trap. An example of a linear Paul trap and its radially confining pseudopotential are shown in Figure 1.

3.2 The Mathieu Equation

The four blades of the Paul trap form an oscillating quadrupole when two opposing blades are connected to a radio frequency (RF) source while the other two blades are grounded or DC biased. As the quadrupole oscillates, the pairs of opposing poles alternate between pushing ions towards the center of the trap and pulling them away creating a hyperbolic electric potential that rotates about the trap axis at the RF drive frequency. Laplace's Equation guarantees that the potential created from this

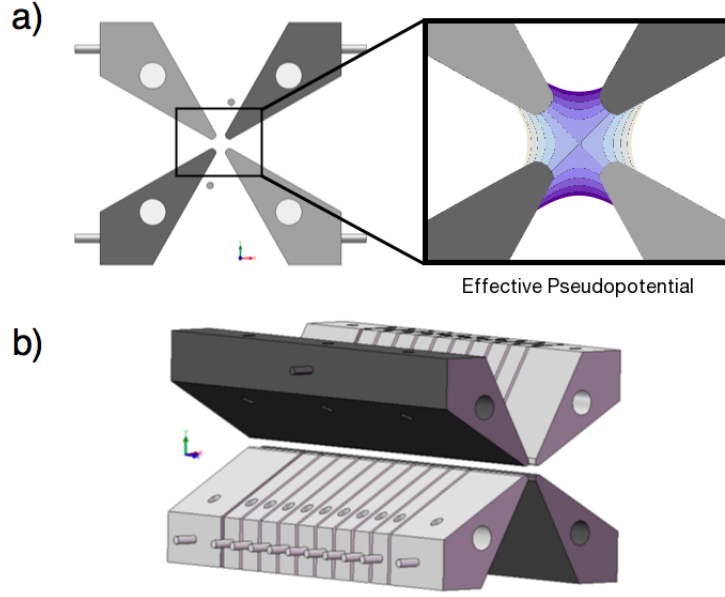


Figure 1: **a)** A cross section of the linear Paul trap used in this paper showing the pondermotive pseudopotentials between electrodes. **b)** A side view of the same trap.

quadrupole must always have the form:

$$\phi = \frac{\phi_0}{r_0^2}(\lambda x^2 + \sigma y^2 + \gamma z^2) \quad (1)$$

where ϕ_0 is the RF drive potential, r_0 is the distance from the tips of the blades to the center of the trap, and λ , σ , and γ are weighting constants [25]. The axial symmetry of linear Paul traps forces $\gamma = 0$; therefore Laplace's Equation is satisfied when $\lambda = -\sigma = 1$. When the potential $v(t) = U_0 + V_0 \cos(\Omega_{rf}t)$ is applied to the RF blades, the electric potential within the trap becomes [25]:

$$\phi = \frac{U_0 + V_0 \cos(\Omega_{rf}t)}{r_0^2}(x^2 - y^2) \quad (2)$$

From Newton's second law, the motion of a singly-ionized atom of mass m in this potential must be governed by:

$$m\ddot{x} + \frac{2xe}{r_0^2}(U_0 + V_0 \cos(\Omega_{rf}t)) = 0 \quad (3)$$

$$m\ddot{y} - \frac{2ye}{r_0^2}(U_0 + V_0 \cos(\Omega_{rf}t)) = 0 \quad (4)$$

Equations 3 and 4 are specific examples of a more general ordinary differential equation called the Mathieu Equation

$$\frac{d^2y}{d^2\xi} + (a - q \cos(2\xi))y = 0 \quad (5)$$

after using the identity $\xi = \frac{\Omega_{rf}t}{2}$ and substituting for a and b [25]. The Mathieu Equation appears to be a simple ordinary differential equation; however, its generality yields many different solution sets. Using the Mathieu Equation to solve for the motion of ions in a pondermotive pseudopotential first requires knowledge about the existence of solutions and how their stability depends on a and b . Once stable solutions are found, it is possible to determine the nature of the periodic orbits of trapped ions in linear Paul traps.

3.3 *Trap Stability*

Ions that become trapped by the RF potential can have only two types of motion. They can be stationary at the trap's center, or they can oscillate periodically around it. Since the stationary solutions are unstable, one must show that periodic solutions to the Mathieu Equation exist and are stable. An initial trial solution to the Mathieu Equation assumes that periodic solutions with periods of π and 2π yields two sets of equations for an m^{th} order solution [26]

$$y = \cos(m\xi) + qc_1(\xi) + q^2c_2(\xi) + q^3c_3(\xi) + \dots \quad (6)$$

$$a = m^2 + \alpha_1q + \alpha_2q^2 + \alpha_3q^3 + \dots \quad (7)$$

and

$$y = \sin(m\xi) + qs_1(\xi) + q^2s_2(\xi) + q^3s_3(\xi) + \dots \quad (8)$$

$$b = m^2 + \beta_1q + \beta_2q^2 + \beta_3q^3 + \dots \quad (9)$$

where each c_i , s_i , α_i , and β_i is iteratively found by solving the Mathieu Equation for all c_j s, s_j s, α_j s, and β_j s where $j < i$. It is convention that b is substituted for a in

Equation 9 to distinguish the sine and cosine solutions, but they both represent the a parameter in the canonical Mathieu Equation. When plotted as level sets in q - a space, these solutions trace out stability and instability domains shown in Figure 2. Solutions for a and b used in Figure 2 are given in Appendix A.

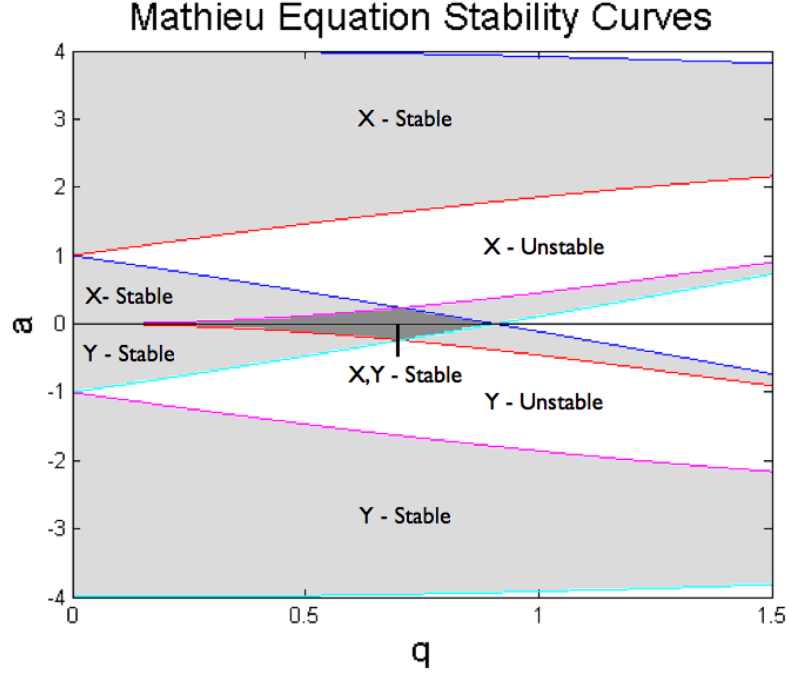


Figure 2: Stability regions of the Mathieu Equation in q - a space. The red and blue lines correspond to a and b solutions to Equations 7 and 9 in the x direction while the magenta and cyan lines correspond to a and b solutions in the y direction. Stable periodic solutions of the form in Equations 6 and 8 exist and are stable in the gray regions while solutions for values of q and a in the white regions are unstable.

3.4 Secular Frequency and Micromotion

Now that stable solutions to the Mathieu Equation have been shown to exist, it is possible to understand particle motion in linear Paul traps. Finding the equations for stable ion motion requires a more general solution to the Mathieu Equation given by the series expansion:

$$y(\xi) = A \sum_{r=-\infty}^{\infty} c_{2r} \cos((2r + \beta)\xi) + B \sum_{r=-\infty}^{\infty} c_{2r} \sin((2r + \beta)\xi) \quad (10)$$

In this form, solving the equations of motion reduces to finding the coefficients A , B , and c_{2r} for an arbitrary $\beta \in (0, 1)$ [26]. Inserting Equation 10 into the Mathieu Equation yields the recurrence relation for the c_{2r} coefficients [15].

$$-\frac{(2r + \beta)^2}{q}c_{2r} + c_{2r-2} + c_{2r+2} = 0 \quad (11)$$

Since the goal is to find stable ion motion, one can restrict β to

$$\beta = \left[a - \frac{(a-1)a^2}{[2(a-1) - q^2]} - \frac{(5a+7)q^4}{32(a-1)^3(a-4)} + O(q^6) \right]^{\frac{1}{2}} - m \quad (12)$$

so that Equation 10 only satisfies the Mathieu Equation in stable regions in q - a space bounded by the m^{th} -order curves a_m and b_{m+1} [26]. One important note about Equation 12 is that it is true for both positive and negative values of q . Inserting Equations 11 and 12 into the general solution yields

$$y(\xi) \simeq Ac_0 \cos(\beta\xi) \left[1 + \frac{q}{2} \cos(2\xi) \right] \quad (13)$$

for values of $|q| \ll 1$ and $a = 0$ [15]. Equation 13 is a simplified, stable solution to the Mathieu Equation for small values of q . Working backwards from the substitutions used to get to the Mathieu Equation from the initial equations of motion in the x - y plane, Equation 13 becomes the system of equations

$$x(t) = Ac_0 \cos(\omega_x t) \left[1 + \frac{q_x}{2} \cos(\Omega_{rf} t) \right] \quad (14)$$

$$y(t) = Ac_0 \cos(\omega_y t) \left[1 + \frac{q_y}{2} \cos(\Omega_{rf} t) \right] \quad (15)$$

for the motion of an ion in a Paul trap. Due to the symmetry of linear Paul traps,

$$\omega_x = \omega_y = \frac{eV_0}{\sqrt{2}m\Omega_{rf}r_0^2}. \quad (16)$$

Under these equations of motion, ions move in periodic orbits about the null of the RF potential at the ‘‘secular frequency’’ ($\omega_{x,y}$) and at the RF drive frequency (Ω_{rf}) [15].

Micromotion is ideally much smaller than motion at the secular frequency because of the assumption that $q \ll 1$ and that there is no DC bias to the RF potential by setting $U_0 = 0$ ($\therefore a_{x,y} = 0$). The ion's orbit will therefore remain periodic, and the ion will stay trapped. Unfortunately, stray electric fields due to small DC biases along the Paul trap and surrounding chamber can occur leading to increased micromotion. If left uncompensated, the micromotion term in Equations 14 and 15 can grow larger than the secular frequency term [27]. Any micromotion will heat the ion until it escapes, but severe micromotion can produce heating rates large enough to prevent trapping.

When static electric fields are added to Equations 3 and 4 and $U_0 \neq 0$, the original systems of equations become:

$$\ddot{x} + [a_x + 2q_x \cos(\Omega_{rf}t)] \frac{\Omega_{rf}^2}{4} x = \frac{q\vec{E}_{DC} \cdot \hat{x}}{m} \quad (17)$$

$$\ddot{y} + [a_y + 2q_y \cos(\Omega_{rf}t)] \frac{\Omega_{rf}^2}{4} y = \frac{q\vec{E}_{DC} \cdot \hat{y}}{m} \quad (18)$$

This leads to a new general solution set

$$x(t) = [u_{0_x} + Ac_0 \cos(\omega_x t + \psi_S)] \left[1 + \frac{q_x}{2} \cos(\Omega_{rf}t) \right] \quad (19)$$

$$y(t) = [u_{0_y} + Ac_0 \cos(\omega_y t + \psi_S)] \left[1 + \frac{q_y}{2} \cos(\Omega_{rf}t) \right] \quad (20)$$

similar to Equations 14 and 15 [27]. General electric fields will can be decomposed onto both x and y axes, so the terms

$$u_{0_x} \simeq \frac{4q\vec{E}_{DC} \cdot \hat{x}}{m(a_x + \frac{1}{2}q_x^2)\Omega_{rf}^2} \quad (21)$$

$$u_{0_y} \simeq \frac{4q\vec{E}_{DC} \cdot \hat{y}}{m(a_y + \frac{1}{2}q_y^2)\Omega_{rf}^2} \quad (22)$$

show that as the stray field increases, the micromotion terms increase until they can become larger than the secular frequency term [27].

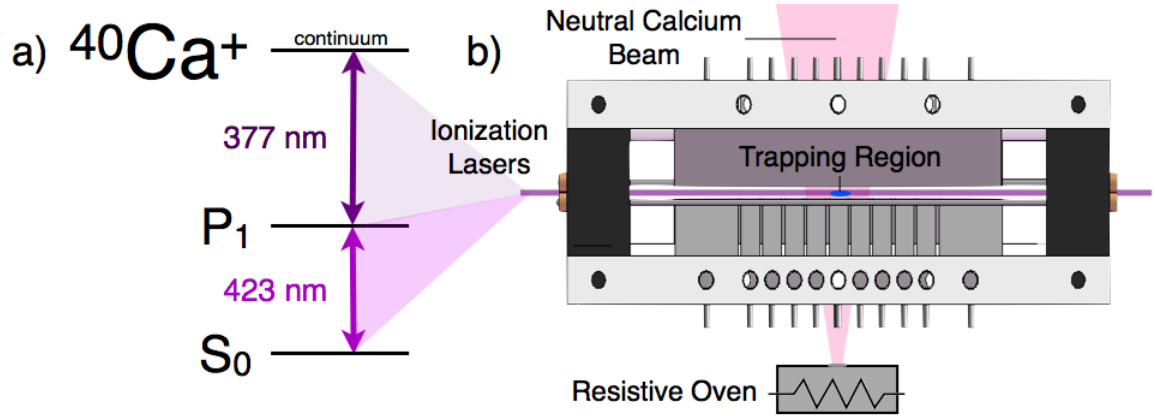


Figure 3: **a)** Two-level ionization scheme for $^{40}\text{Ca}^+$. **b)** A diagram of how the neutral ^{40}Ca beam is generated by the resistive oven, passed through the trap, and is hit by the ionization lasers to load $^{40}\text{Ca}^+$ ions.

3.5 Loading $^{40}\text{Ca}^+$

Creating ions that can be trapped relies on ionizing a beam of neutral atoms as it passes through a linear Paul trap (shown in Figure 3). Calcium metal is atomized in the ultra-high-vacuum environment of the ion trap by using a resistively heated oven. When the calcium metal is hot enough, it sublimates through a hole in the oven towards the trap. The calcium sample produces different calcium isotopes where 96.9% will be $^{40}\text{Ca}^+$, 2.04% will be $^{44}\text{Ca}^+$, and the rest will be other isotopes with mass numbers of 42, 43, 46, and 48 [28]. Atoms that pass through the trap intersect with co-aligned 423 nm and 377 nm radiation are ionized by the two-level ionization and then become trapped in the center of the RF and DC trapping potentials. Each isotope will have a different hyperfine shift on the 423 nm transition which allows for selective isotope loading.

CHAPTER IV

CALCIUM ION QUBITS

4.1 *The Electronic Structure of $^{40}\text{Ca}^+$*

Quantum information can be stored in the electronic or nuclear state of trapped ions. Quantum computation with atomic nuclei require nuclear magnetic resonance techniques which will not be presented here [29]. Many electron transitions in can be easily driven by visible radiation. Using the valence electron orbitals for quantum computation first requires lifting the degeneracies of the electronic states of interest. Figure 4 shows the $^{40}\text{Ca}^+$ transitions used in this experiment with the fine structure shifts [30]. The most important transitions are the 397 nm, Doppler cooling, transition and the 866 nm, re-pumping, transition which are responsible for keeping the ion from overheating and escaping once trapped. The two-level qubit transition used for all quantum computation and sideband cooling is the 729 nm transition depicted in Figure 4 by the $|0\rangle$ and $|1\rangle$ symbols. Re-pumping out of the $D_{5/2}$ state by the 854 nm transition moves any $D_{5/2}$ population to the $P_{3/2}$ state where the branching ratio between the $P_{3/2} \rightarrow D_{5/2}$ and $P_{3/2} \rightarrow S_{1/2}$ transitions statistically force any spontaneous decay to fall back to the $S_{1/2}$ state. Even if the ion falls back to the $D_{5/2}$ state, it is pumped to the $P_{3/2}$ state until in eventually decays. The 393 nm transition is not optically pumped because the predominately one-sided branching ratio makes the 393 nm transition ideally suited for qubit state detection and sideband cooling after 854 nm re-pumping.

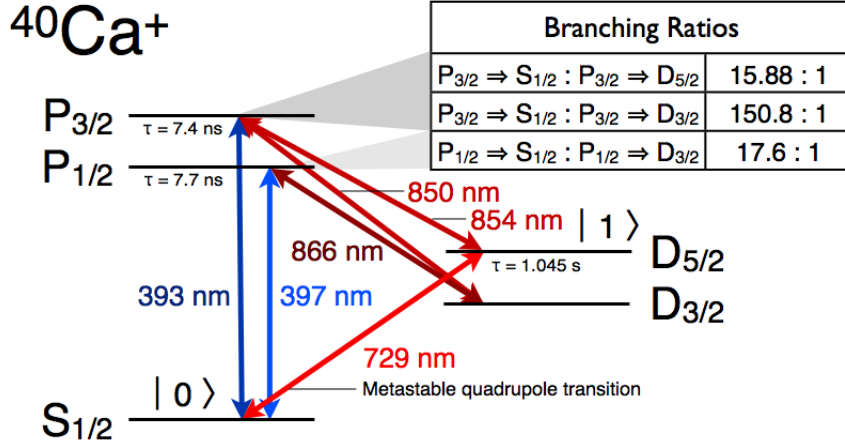


Figure 4: Primary transitions necessary for implementing quantum logic, Doppler cooling, and sideband cooling on $^{40}\text{Ca}^+$ ions. Branching ratios between $P \rightarrow S$ and $P \rightarrow D$ transitions and the mean lifetime τ for spontaneous decay back to the $S_{1/2}$ level are also shown. The 729 transition is used to change the state of the $^{40}\text{Ca}^+$ qubit by shifting probability densities between the $|1\rangle$ and $|0\rangle$ states [30].

4.2 Doppler Cooling

Immediately after ions are trapped, they begin to heat from interactions with their surroundings. This includes external radiation from equipment or isolated dipoles and micromotion from stray fields or patch potentials on the trap [13, 14]. When a moving ion interacts with electromagnetic radiation, this radiation appears Doppler shifted in the ion's reference frame; therefore, the radiation must be detuned in order to excite a transition. Consider a $^{40}\text{Ca}^+$ ion moving with a constant velocity antiparallel to the propagation vector of monochromatic, 397 nm radiation. In order to excite the $S_{1/2} \rightarrow P_{1/2}$ transition, the 397 nm radiation must be red-detuned to a longer wavelength so that, in the ion's reference frame, it is Doppler shifted blue to the correct frequency, allowing the ion to absorb the radiation (Figure 5). Photons carry momentum, so immediately after the ion absorbs the photon and makes a transition, its velocity is reduced slightly. The ion will then receive a momentum boost from spontaneous

emission that can occur in any direction. When the momentum kicks from randomly-oriented spontaneous emission are time averaged, the net result is no momentum gain since the sum of all vectors over the unit sphere is zero. Importantly, the momentum kicks from the Doppler shifted radiation are always in the same direction; therefore, the net effect reduces the velocity of the ion. This is the mechanism behind Doppler cooling.

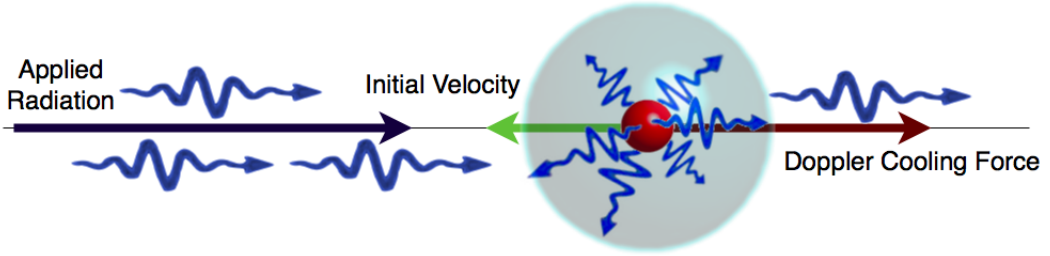


Figure 5: The incident, red-detuned photons are blue-shifted in the ion’s reference frame back to the proper frequency to drive a transition.

There is a limit to how cold a cloud of ions can get with just Doppler cooling. For a 1D cloud of ions with temperature T , the distribution of ion velocities within the gas is given by the Maxwell-Boltzmann distribution

$$f(v) = \sqrt{\frac{M}{2\pi k_B T}} e^{-\frac{Mv^2}{2k_B T}}, \quad (23)$$

and the motion is governed by the forces each ion receives from constant absorption (F_c) and sporadic emission (F_v) of radiation:

$$F(p, t) = F_c(p, t) + F_v(p, t) \quad [31]. \quad (24)$$

Like before, the time average of this force is only the constant recoil force from photon absorption:

$$\langle F(p, t) \rangle = \langle F_c(p, t) \rangle + 0. \quad (25)$$

Both forces result in a random walk process in momentum space given by $W(p, t)$ where the ion periodically loses momentum after absorption and gains momentum

after emission. Equation 25 forces the ion's random momentum walk to have the net effect of reducing the ion's overall momentum. The time rate of change in $W(p, t)$ is given by a Taylor expansion

$$\frac{\partial W(p, t)}{\partial t} = \frac{\partial [M_1 W(p, t)]}{\partial p} + \frac{1}{2} \left[\frac{\partial^2 [M_2 W(p, t)]}{\partial p^2} \right] + \dots \quad (26)$$

where M_1 and M_2 ,

$$M_1 = \langle F(p, t) \rangle = \langle F_c(p, t) \rangle \quad (27)$$

$$M_2 = \langle F_v(p, t') F_v(p, t'') \rangle = 2D(p, t) \delta(t' - t''), \quad (28)$$

are the first and second moments of the random walk process and $D(p, t)$ is the 1D gas diffusion function [31]. Equations 26 through 28 combine to yield,

$$\frac{\partial W(p, t)}{\partial t} = \frac{\partial [F_c(p, t) W(p, t)]}{\partial p} + \frac{1}{2} \left[\frac{\partial^2 [D(p, t) W(p, t)]}{\partial p^2} \right], \quad (29)$$

the Fokker-Planck Equation.

The simplest case for Doppler cooling is when the diffusion term,

$$D(p, t) = D_0 = \frac{s\gamma(\hbar k)^2}{2}, \quad (30)$$

is a constant determined by the transition's decay rate γ , the saturation parameter s , the wavenumber k and the Doppler cooling term,

$$F_c(p, t) = -\beta v = -\hbar k^2 s v, \quad (31)$$

which is proportional to the ion's velocity [31]. The saturation parameter in Equations 30 and 31,

$$s = \frac{|\Omega|^2}{2|\frac{\gamma}{2} - i\delta|^2}, \quad (32)$$

is determined by the transition's Rabi frequency, Ω , which will be properly defined later, decay rate γ , and the frequency detuning, δ , of the incident radiation [31]. Under

the constant diffusion and velocity-dependent Doppler force assumptions, Equation 29 has a steady-state solution,

$$\bar{W}(p) \propto e^{-\frac{\beta p^2}{2MD_0}}, \quad (33)$$

whose general form is identical to the Maxwell-Boltzmann distribution with a characteristic temperature,

$$k_B T_D = \frac{D_0}{\beta} = \frac{\hbar\gamma}{2}, \quad (34)$$

proportional to the atomic transition's energy band width [31]. This is the Doppler cooling limit because any detuning of the incident radiation within the natural linewidth of a transition will not have any further cooling effect. Another temperature limit,

$$k_B T_R = \frac{\hbar^2 k^2}{M}, \quad (35)$$

is proportional to the momentum each incident photon carried. This momentum becomes the minimum threshold because the photons cannot remove less momentum from the ion than they intrinsically have, and is called the optical cooling limit [31]. As hot ions are Doppler cooled, the ion's scattering fluorescence rate grows to a peak before flattening off [32]. When the scattered fluorescence rate becomes constant, the Doppler cooling rate is either close to the Doppler cooling limit or equal to the heating rate of the ion due to its surroundings.

4.3 *Qubits and Rabi Transitions*

A two-level system is the simplest quantum mechanical system that can be used to implement quantum computations. In $^{40}\text{Ca}^+$ ions, the two qubit levels are the $S_{1/2}$ ground state $|g\rangle$ and the $D_{5/2}$ excited state $|e\rangle$ (also denoted as the $|0\rangle$ and $|1\rangle$ states). Because electrons are quantum mechanical, they do not classically occupy one specific location until they are measured. Instead, their position is described by a spatial probability density function: the electron's wavefunction. Unlike a state in a classical

computer which can only be 0 or 1, the quantum nature of the electron allows it to occupy both $|g\rangle$ and $|e\rangle$ states with different probabilities simultaneously [33]. This is the basis of quantum computing and quantum information storage. Information is stored in the electron's wavefunction as it exists between the two states and is not stored in the states themselves. When an observer wants to measure the state of a prepared quantum system, however, it is impossible to get the relative probabilities of the electron being in each state because the act of measuring the quantum system collapses the information stored in the electron's wavefunction to either the $|g\rangle$ or $|e\rangle$ state. Mapping out the relative probability densities of a prepared quantum system requires repeatedly preparing and measuring the system to calculate the probabilities of the electron being in either the $|g\rangle$ or $|e\rangle$ states.

Rabi transitions describe how the electron population is shifted between the two levels of the $^{40}\text{Ca}^+$ qubit. If we assume that our two-level system is complete and that each state is an eigenfunction of some Hamiltonian \mathbf{H}_0 , then the time-independent Schrödinger Equation yields

$$\hat{H}_0|g\rangle = E_g|g\rangle \tag{36}$$

$$\hat{H}_0|e\rangle = E_e|e\rangle \tag{37}$$

where the states

$$\langle g|e\rangle = \delta_{eg} \tag{38}$$

are orthonormal [34]. Completeness implies that any general state of this system can be expressed as a linear combination of these two qubit states,

$$|\Psi\rangle = \alpha|g\rangle + \beta|e\rangle, \tag{39}$$

where the probabilities of finding the particle in either state must sum to 1 because the particle cannot exist outside these two states $|\alpha|^2 + |\beta|^2 = 1$. The general solution

to the time-dependent Schrödinger Equation is:

$$|\Psi(t)\rangle = \alpha(t)|g\rangle e^{-\frac{iE_g t}{\hbar}} + \beta(t)|e\rangle e^{-\frac{iE_e t}{\hbar}}. \quad (40)$$

This solution can be decomposed into these two basis states where the coefficients α and β are now time-dependent [34]. If the system were left alone, any initial conditions would require that $\alpha(t)$ and $\beta(t)$ remain constant; however, the presence of a time-dependent, electromagnetic field of the form $\vec{E}(\vec{r}, t) = E_0 \hat{e} \cos(\vec{k}_l \cdot \vec{r} - \omega_l t)$ causes mixing of the $\alpha(t)$ and $\beta(t)$ coefficients. The original Hamiltonian of the two-level system

$$\hat{H} = \hat{H}_0 - e\vec{E}(\vec{r}, t) \cdot \vec{r} \quad (41)$$

$$= \hat{H}_0 + \hat{H}'(t) \quad (42)$$

is now perturbed by the electromagnetic radiation under the dipole approximation [31]. Substituting Equations 40 and 42 into the time-dependent Schrödinger Equation, we find

$$\alpha(t) \left[\hat{H}'|g\rangle \right] e^{-\frac{iE_g t}{\hbar}} + \beta(t) \left[\hat{H}'|e\rangle \right] e^{-\frac{iE_e t}{\hbar}} = i\hbar \left[\dot{\alpha}(t)|g\rangle e^{-\frac{iE_g t}{\hbar}} + \dot{\beta}(t)|e\rangle e^{-\frac{iE_e t}{\hbar}} \right]. \quad (43)$$

Setting $\omega_0 = \frac{E_e - E_g}{\hbar}$,

$$\alpha(t) = -\frac{i}{\hbar} \int_0^t \left[\alpha_0 H'_{gg} + \beta_0 H'_{ge} e^{-i\omega_0 t'} \right] dt' \quad (44)$$

$$\beta(t) = -\frac{i}{\hbar} \int_0^t \left[\beta_0 H'_{ee} + \alpha_0 H'_{eg} e^{i\omega_0 t'} \right] dt' \quad (45)$$

the first-order time-dependent perturbation theory solutions for $\alpha(t)$ and $\beta(t)$ given the initial population densities α_0 and β_0 [34]. If the two-level system starts out with the electron completely in the ground state ($\alpha_0 = 1$ and $\beta_0 = 0$), the time-dependent probability density of finding the electron in the excited state is

$$\beta(t) \simeq -i\Omega \int_0^t \cos(\omega_l t') e^{i\omega_0 t'} dt' \quad (46)$$

$$= -\frac{\Omega}{2} \left[\frac{e^{i(\omega_0 + \omega_l)t} - 1}{\omega_0 + \omega_l} + \frac{e^{i(\omega_0 - \omega_l)t} - 1}{\omega_0 - \omega_l} \right] \quad (47)$$

$$= -i\frac{\Omega}{\Omega'} \sin\left(\frac{\Omega' t}{2}\right) e^{-\frac{i\delta t}{2}} \quad (48)$$

where the Rabi frequency is given by

$$\Omega = -\frac{eE_0}{\hbar} \langle e|r|g \rangle \quad (49)$$

and

$$\Omega' = \sqrt{\Omega^2 + \delta^2} \quad (50)$$

is the frequency of probability density oscillations between the $|g\rangle$ and $|e\rangle$ states assuming that the radiation detuning δ is small compared to the transition frequency ($\delta = |\omega_0 - \omega_l \ll \omega_0 + \omega_l$) [31, 34]. The probability of finding the electron in the excited state is now

$$P_{g \rightarrow e} = \frac{\Omega^2}{\Omega'^2} \sin^2 \left(\frac{\Omega' t}{2} \right). \quad (51)$$

This equation shows that the probability of finding an electron in the excited state oscillates between 0 and $\frac{\Omega^2}{\Omega'^2}$ depending on the laser detuning.

For small detuning ($\delta \ll 1$), a laser pulse with a duration $t = \frac{1}{2\Omega'}$ completely shifts the electron probability from the ground state to the excited state. This is called a π pulse since it corresponds to a rotation in phase space by π radians. Likewise, an on-resonance laser pulse of duration $t = \frac{1}{4\Omega'}$ on a two-level system initially in the ground state transfers 50% of the probability density from the ground state to the excited state and is called a $\pi/2$ pulse. Implementing these pulses on $^{40}\text{Ca}^+$ qubits requires very precise 729 nm laser tuning and pulse control so that the populations get shifted exactly to the desired values. Any temporal or frequency error will result in improper probability density transfer and will lead to errors with implementing quantum gates or storing quantum information.

4.4 *Sideband Cooling*

To understand the basic elements of the $^{40}\text{Ca}^+$ qubit, the previous Hamiltonian omitted many necessary components. Ions confined to move in the parabolic pseudopotential of a linear Paul trap behave like quantum harmonic oscillators. Adding

a quantum harmonic oscillator to the 1D Hamiltonian presented earlier and properly defining \hat{H}_0 and \hat{H}' in terms of the Pauli spin matrices

$$\hat{H}_0 = \hbar\omega_x(\hat{a}^\dagger\hat{a} - \frac{1}{2}) + \frac{1}{2}\hbar\omega_0\hat{\sigma} \quad (52)$$

$$\hat{H}' = \frac{1}{2}\hbar\Omega(\hat{\sigma}_+ + \hat{\sigma}_-)\left(e^{i(\vec{k}_l \cdot \hat{x} - \omega_l t)} + e^{-i(\vec{k}_l \cdot \hat{x} - \omega_l t)}\right) \quad (53)$$

$$= \frac{1}{2}\hbar\Omega\left(e^{i\eta(\hat{a} + \hat{a}^\dagger)}\hat{\sigma}_+e^{-i\omega_l t} + e^{-i\eta(\hat{a} + \hat{a}^\dagger)}\hat{\sigma}_-e^{i\omega_l t}\right) \quad (54)$$

produces the complete 1D Hamiltonian where

$$\eta = k \cos(\phi) \sqrt{\frac{\hbar}{2m\omega_x}} \quad (55)$$

is the Lamb-Dicke coupling parameter for a laser making an angle ϕ to the axis of the quantum harmonic oscillator [30]. Unlike the original \hat{H}' which was only responsible for shifting population densities between the $|g\rangle$ and $|e\rangle$ states, this new \hat{H}' shifts population densities between the $|g, n\rangle$ and $|e, n'\rangle$ states where n, n' are vibrational quantum numbers for the quantum harmonic oscillator. Figure 6 shows how this process happens in the $^{40}\text{Ca}^+$ qubit.

By detuning the 729 nm laser to $\omega_l - \omega_x$, it is possible to shift population from the $|S_{1/2}, n\rangle$ state to the $|D_{5/2}, n - 1\rangle$ state thereby reducing the ion's vibrational energy in the quantum harmonic oscillator. If the 729 nm laser were turned off, the electron would eventually decay to the $|S_{1/2}, n - 1\rangle$, but this would take 1.045s. Pumping any population from the $|D_{5/2}, n - 1\rangle$ to the $|P_{3/2}, n - 1\rangle$ with an on-resonance 854 nm transition allows the electron to spontaneously decay to the $|S_{1/2}, n - 1\rangle$ internal ground state with 1 less quanta of motional energy on the order of nanoseconds. Repeating this cycle continuously removes vibrational quanta until the ion is left in its vibrational ground state or until the sideband cooling rate equals the trap heating rate.

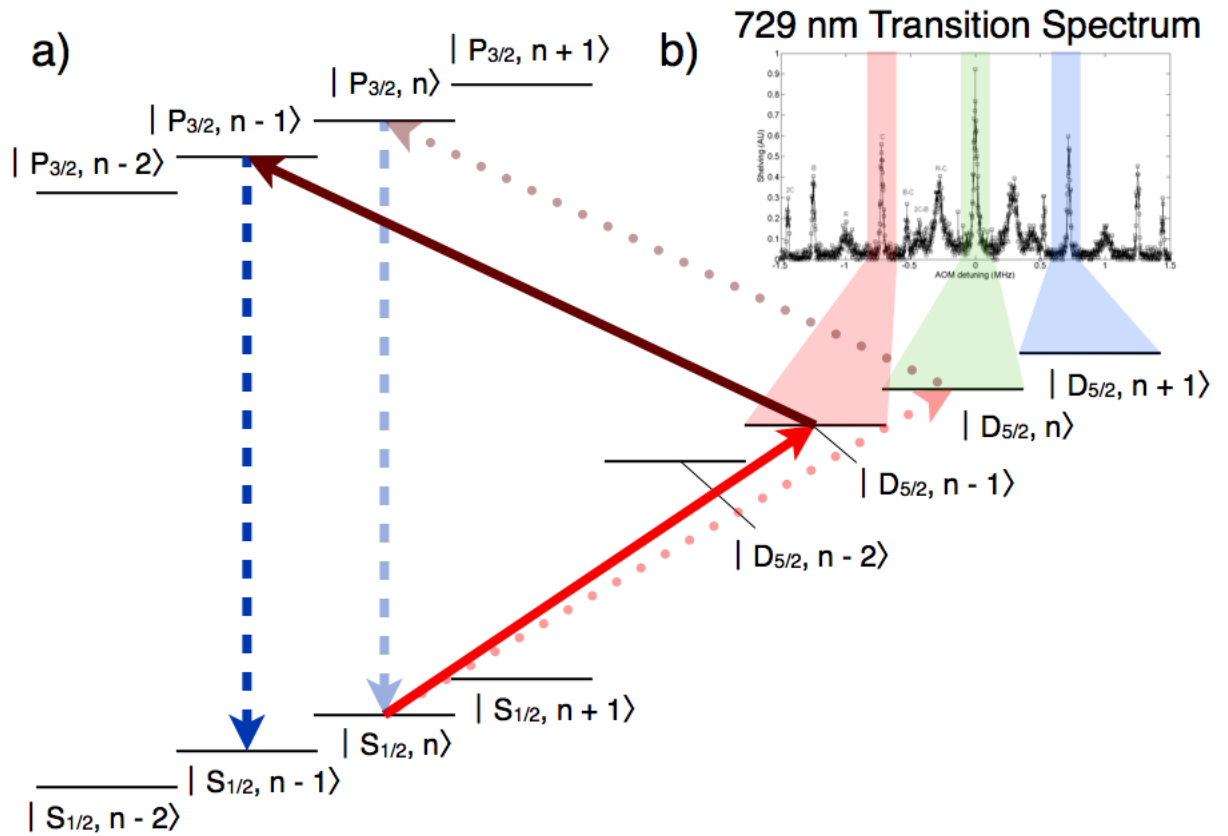


Figure 6: a) The detuned 729 nm and a resonant 854 nm laser transitions with 393 nm spontaneous emission used for sideband cooling $^{40}\text{Ca}^+$. b) A 729 nm transition spectrum shows the red (cooler) sideband, carrier transition, and the blue (hotter) sideband

CHAPTER V

CONTROL INTERFACE

5.1 Acousto-Optic Modulators

Manipulating laser frequencies and intensities for trapping, cooling, and implementing quantum gates requires the use of Acousto-Optic Modulators (AOMs). AOMs work by creating density waves inside an optical crystal by vibrating it at radio frequencies. As photons pass through the RF wave, they can receive a momentum kick if conditions are just right inside the crystal. Photons that interact with the RF wave leave the crystal with a frequency equal to that of the applied radio frequency added to the photon's initial frequency due to the conservation of energy and leave with a different propagation direction due to the conservation of momentum. Changing the propagation of the incident beam is important because it allows for fast shuttering of a laser beam's intensity as the beam becomes coupled and decoupled from any optics downstream of the AOM. A demonstration AOM is shown in the first part of Figure 7. It is theoretically possible to use feedback loops from an external cavity or other measurement devices to tune laser output frequencies directly, but the response times of these loops are usually slow, prohibit multiple experiments from using the same laser, and such a scheme could cause the laser to jump from the intended lasing mode. Figure 8 shows the complete 397 nm laser control setup including the lasers, AOMs, control electronics, and other optical elements.

There are two regimes used for analyzing the diffraction pattern created by AOMs: the Raman-Nath regime and the Bragg regime. In the Raman-Nath regime, the optical crystal in the AOM is treated as a thin optical element, and the applied RF power is large compared to the incident laser power. The Bragg regime assumes a

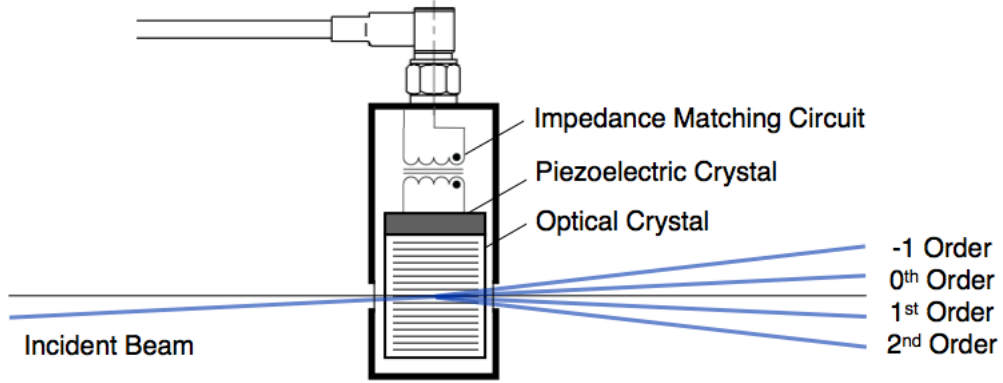


Figure 7: An example AOM showing the incident beam, excitant orders, internal impedance matching circuit, and piezoelectric and optical crystals with internal traveling wave.

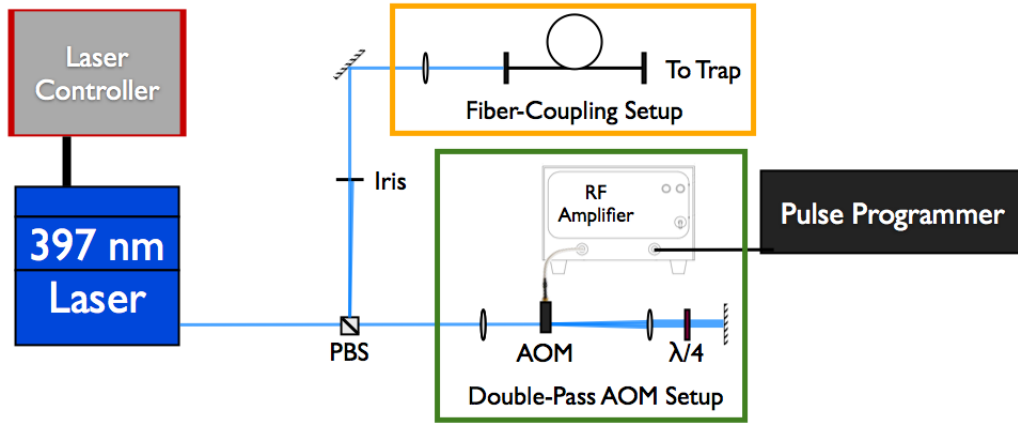


Figure 8: Complete 397 nm laser setup

larger crystal with smaller density variations from lower RF amplitude. Most AOMs operate in the Bragg regime since a higher percentage of the incident wave interacts with the applied RF density wave [35]. Both regimes start with the principle that the RF wave propagating through the optical crystal produces a spatial variation in the index of refraction such that

$$n(x) = n_0 + \delta n \cos(k_{rf}x - \omega_{rf}t) \quad (56)$$

where δn is related to the applied RF power

$$M \frac{P_{rf}}{zh} = \frac{2(\delta n)^2}{n_0^2} \quad (57)$$

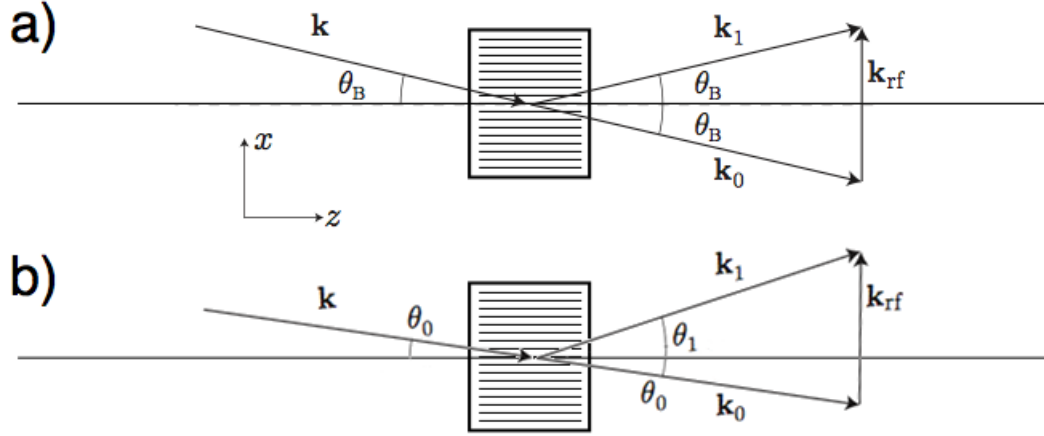


Figure 9: **a)** The ideal AOM Bragg condition with the Bragg angle θ_B . **b)** A general condition for the AOM diffraction where $|\theta_0| + |\theta_1| = 2\theta_B$ [35].

through the figure of merit M , interaction length z , and crystal height h [35]. Photons that interact with this periodic index of refraction pattern to the first order must also satisfy the Bragg condition

$$\lambda_{laser} = 2\lambda_{rf} \sin(\theta_B) \quad (58)$$

which (Figure 9) implies that the optimum angle of incidence is the Bragg angle θ_B and that the diffracted beam will make an angle of $2\theta_B$ to the incident beam. A more general condition is also shown in Figure 9, but the Bragg condition still holds to force $|\theta_0 + \theta_1| = \theta_B$ [35]. Combining the total change in phase

$$d\phi_{0,1} = \frac{n}{n_0} k dr_{0,1} = \frac{k dz}{n_0 \cos(\theta_{0,1})} [n_0 + \delta n \cos(k_{rf} x - \omega_{rf} t)] \quad (59)$$

and differential phase change

$$\frac{\partial \phi_{0,1}}{\partial z} = \frac{k}{\cos(\theta_{0,1})} + \frac{k \delta n}{2n_0 \cos(\theta_{0,1})} [e^{i(k_{rf} x - \omega_{rf} t)} + e^{-i(k_{rf} x - \omega_{rf} t)}] \quad (60)$$

$$= \kappa_{0,1} + \frac{\Omega}{2} [e^{i(k_{rf} x - \omega_{rf} t)} + e^{-i(k_{rf} x - \omega_{rf} t)}] \quad (61)$$

for each path and the vector sum of the incident and excitant electric fields

$$E(z, t) = E(k_0, z)e^{-i\omega_0 t} + E(k_1, z)e^{-i\omega_1 t}, \quad (62)$$

it can be shown that the intensity of the first order diffracted beam

$$I_1 = I_{in} \sin^2 \left(\frac{\Omega z}{2} \right) \quad (63)$$

is a function of the incident and Bragg angles θ_0 and θ_B . When the incident angle is exactly equal to the Bragg angle θ_B , the intensity of the first order beam

$$I_1 = I_{in} = \sin^2 \left(\frac{k\delta n}{2n_0 \cos(\theta_B)} \right) \quad (64)$$

is maximized [35].

5.2 *Direct Digital Synthesizers*

Direct Digital Synthesizers (DDSs) are programmable function generators used to produce waveforms from DC to hundreds of megahertz used to power AOMs in our experiments. The output of a DDS usually has to be amplified like in Figure 8, but this is not always the case. There are the three core parts of every DDS: a phase accumulator, a lookup table, and an output digital-to-analog converter (DAC). Figure 10 shows a block diagram common to most DDS designs and how these pieces are incorporated into an example chip.

The phase accumulator is a clocked adder whose width defines the upper limit of frequency accuracy for the DDS. On the rising edge of the core system clock, the frequency tuning word is added to the value stored in this accumulator. This incrementally increases the stored phase value until it overflows the phase accumulator. The overflow bit is ignored, so the output of the phase accumulator creates a digitized, stepped triangle wave fixed between 0 and the accumulator's maximum value [36]. A phase tuning word can be added to the output of the phase accumulator to augment the accumulators phase relationship to the core system clock. Most of the

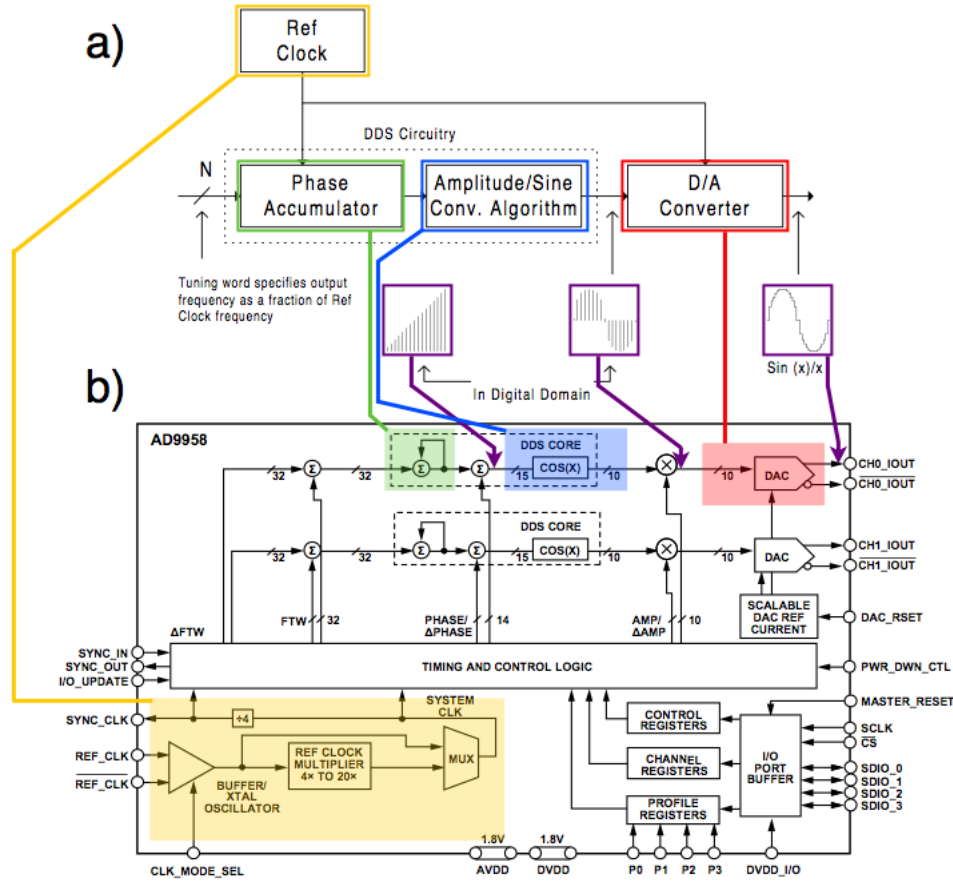


Figure 10: **a)** A block diagram of the internal mechanism common to most DDSs. **b)** An example circuit to show how the core pieces are incorporated into a real DDS. Both images are from Analog Devices [36, 37]

output bits of the phase accumulator are ignored when fed into the look-up table to reduce the amount of memory used by the device. Reducing the bits from the phase accumulator does not reduce the frequency precision of the device, but it does reduce the voltage precision of the final output. The look-up table converts the phase bits to a sine wave, a cosine wave, or, depending on the device, a user-defined waveform [36]. Since the stored look-up table waveforms have constant amplitudes, the output must be multiplied by an amplitude scale factor before being applied to the output DAC. Finally, the output DAC converts the reduced digital signal to a bidirectional current output that is transformed into a 50Ω impedance voltage source. Augmenting the frequency tuning word, phase offset word, and amplitude scale factor allows the user

to precisely control waveforms that can be applied to AOMs for precise, flexible laser control.

laser powers and shape multi-laser pulse sequences using AOMs.

5.3 *FPGA Microarchitecture*

Most of the control structure for implementing quantum gates revolves around controlling the ion trap, controlling lasers, and recording data. Since all of the laser properties are controlled by external DDS modules, the primary elements in the FPGA architecture are synchronized modules that each control one DDS board. These module controllers continuously manipulate the DDS's outputs to create the different laser pulses necessary for implementing an experiment. An internal microcontroller coordinates how these modules execute individual laser pulses into a whole experimental ensemble by sending data over a 36-bit backplane. Data from an experiment, new module pulse sequences, and microcontroller programs are transferred over a computer interface built around the Opal Kelly Front Panel interface. Figure 11 shows a block form of the internal circuitry implemented on the FPGA. Modules can also control DACs, record photon counts, and read voltage data from Analog-to-Digital Converters (ADCs). The key idea is that they are supposed to be customizable to fit the needs of any particular experiment. The FPGA internal structure and immediate supporting electronics like DDS, DAC, and ADC are packaged together in one piece of hardware called the Pulse Programmer.

The embedded microcontroller inside of the Pulse Programmer handles lower priority timing and data management tasks while running an experiment. Due to its single processing pipeline, the main purpose of the microcontroller is to serialize large blocks of parallel pulse sequence data executed by the module controllers into experiments with wait blocks, execution blocks, and data read/write blocks. Keeping with the modular theme of the Pulse Programmer, different microcontrollers can also be

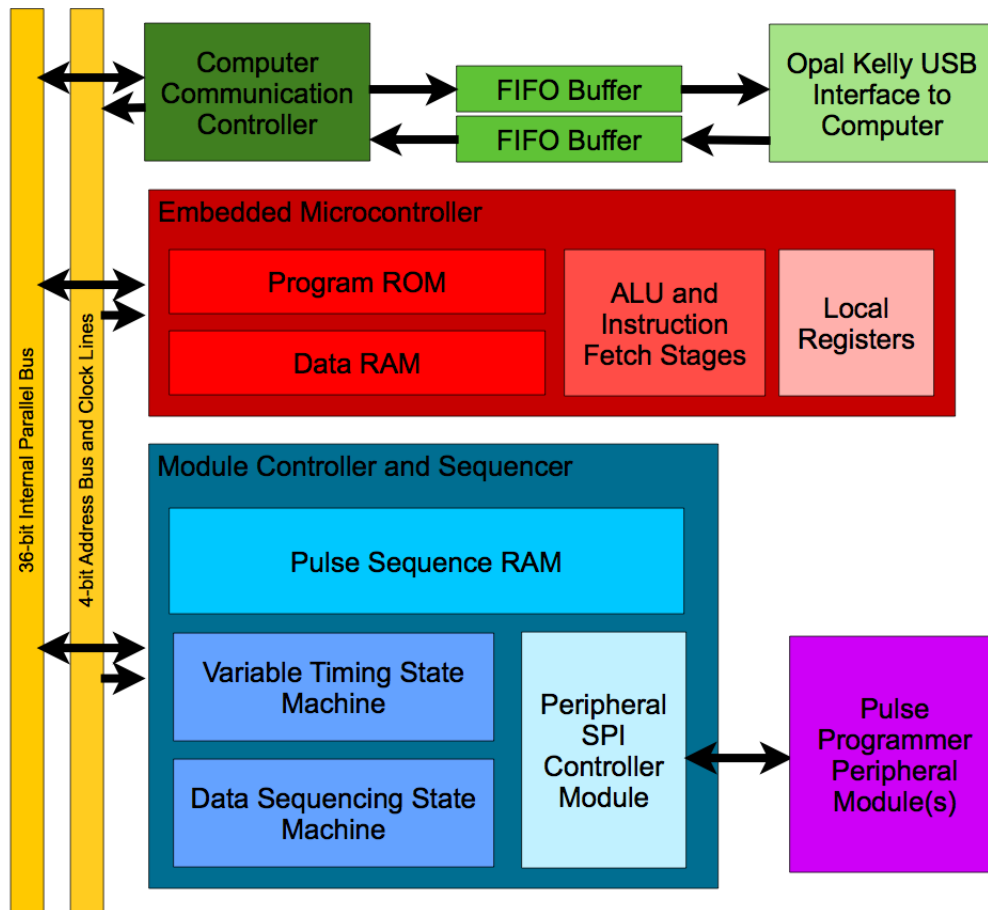


Figure 11: Internal structure of the FPGA showing the primary data bus, clock busses, computer interface, verilog microcontroller, and parallel bank of module controllers

substituted into the Pulse Programmer architecture for different effects. Like substituting module controllers, the only limit to substituting microcontrollers is that the control program syntax must be changed to accommodate every new microcontroller architecture. Another key attribute of the microcontroller is that it is meant to be very general in its capabilities so that the experimenter can create and execute a wide range of experiments.

The module controllers are where the heavy lifting in the Pulse Programmer takes place. Within each module, high speed timers synchronized to a master clock index through data to be sent to or read from peripheral modules at a variable rate. Pulse sequences are written to the internal RAM banks of the modules via the computer interface and data bus to specify what commands to send to their peripheral module(s) and exactly how many core clock cycles to wait before sending each command. Module controllers can also record data by filling up their memories at variable time intervals with experimental data. Once the commands and time intervals are stored into ram, a single trigger initiates all module controllers to send commands or record data in parallel lockstep with each other. Locking multiple module controllers together allows multiple AOMs to be controlled in parallel creating the laser pulse sequences necessary for implementing quantum gates with trapped ions. By moving the critical experimental timing to the module controllers, a higher level of experimental timing accuracy can be achieved, and the embedded microcontroller is now free to process information or communicate with the host system during an experiment.

CHAPTER VI

$^{40}\text{Ca}^+$ SPECTROSCOPY

6.1 AOM Power Scan

Before trapping ions with the Pulse Programmer, it was first tested by performing AOM power scans. When running an experiment, it is very important that the laser power to the trap stays as constant as possible while scanning frequencies since fluorescence is related to laser detuning and saturation. The data shown in Figure 12 was taken by varying the RF frequency and amplitude with the Pulse Programmer while recording the transmitted laser power through the AOM. It shows that the AOM achieved a maximum conversion efficiency around 115 MHz and that the transmitted power is roughly constant between 102 MHz and 125 MHz. Outside this region, the power dropoff may be too great for experiments that require low laser powers like reheating rate or Rabi transition measurements. Characterizing the AOM's transmission performance also allows one to determine if the AOM is applying artifacts to any fluorescence measurements.

6.2 $^{40}\text{Ca}^+$ 397 nm and 729 nm Transition Spectroscopy

Transition spectroscopy measurements are the simplest experiments that demonstrate the Pulse Programmer's abilities. Accurate 397 nm and 729 nm transition spectra are necessary for finding the optimal Doppler cooling and sideband cooling frequencies. Since the 866 nm and 854 nm re-pumping lasers do not require high frequency precision, there is no need to measure the spectra for these transitions. Like the AOM power scan, the Pulse Programmer needs to scan through a range of AOM frequencies; however, the lasers must also be pulsed for Doppler cooling loops,

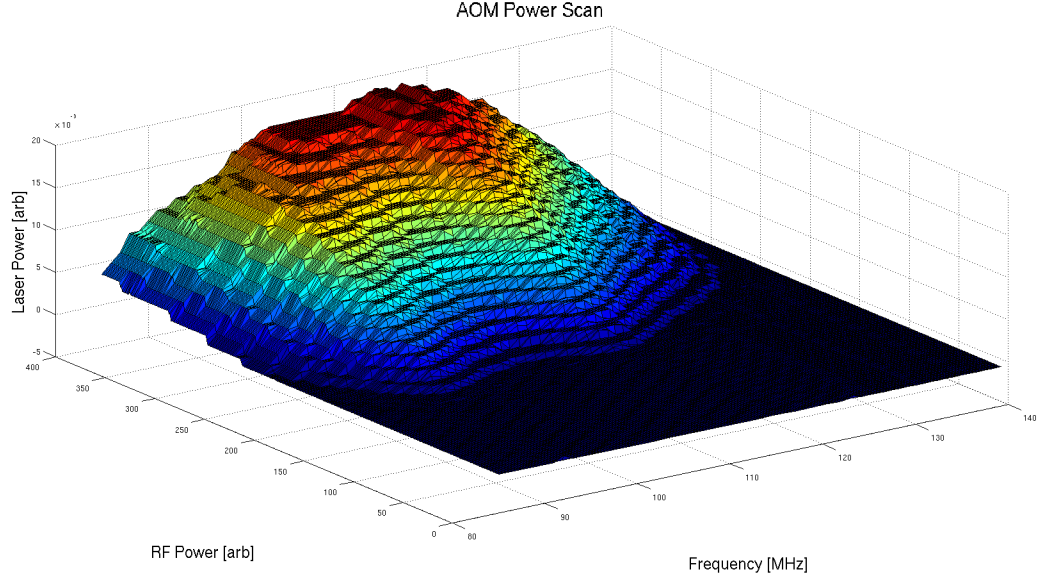


Figure 12: 397 nm laser transmission power as a function of RF frequency and amplitude

state preparation, and fluorescence measurements. These pulses typically range from a few microseconds to less than ten milliseconds.

Figure 13 shows 397 nm and 729 nm transition spectra collected with the Pulse Programmer. The 397 nm transition data was taken by pulsing the 397 nm AOM between 115 MHz for 1 ms of Doppler cooling and 100-135 MHz for 3 ms of fluorescence measurements. Each blue line is an individual scan where every point is the average of 100 runs, and the red line is an average of 6 scans. Maximum fluorescence occurs around 123 MHz; however, this would be a poor place for Doppler cooling because any positive frequency drift in the 397 nm laser would pass over the fluorescence peak and start heating the ion. Optimal cooling occurs at where the slope of the transition spectrum is steepest. This should occur $\gamma/2$ MHz from the center of the transition (11 MHz for $^{40}\text{Ca}^+$); however, the 397 nm AOM is double-passed, so the maximum slope occurs 5.5 MHz from the center of the transition. The 729 nm scan was taken in an identical manner to the 397 nm scan and shows eight of the possible transitions from the $S_{1/2}$ state to the $D_{5/2}$ state with Zeeman splitting. The Zeeman scan is

important for finding the frequency of the $S_{1/2}, m_j = -1/2$ to the $D_{5/2}, m_j = -5/2$ transition which is the optimal transition for sideband cooling and Rabi transitions because there is no way for the electron to fall into the dark $S_{1/2}, m_j = +1/2$ state.

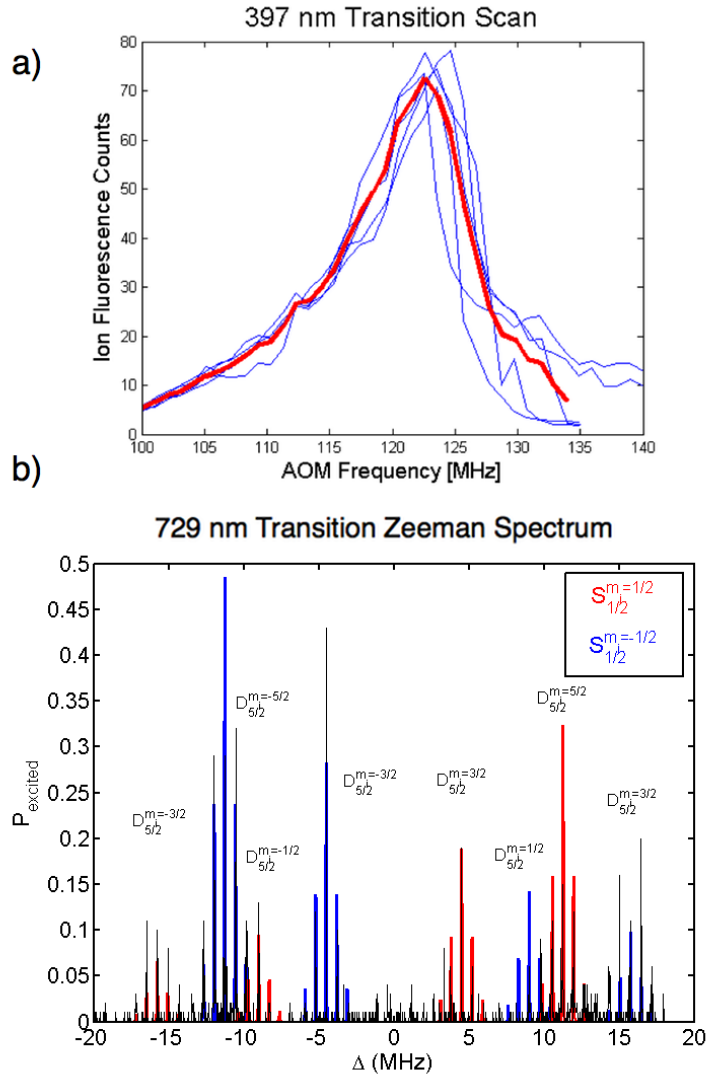


Figure 13: **a)** 397 nm transition spectrum. Every data point on the six scans (blue) are the averages of 100 runs, and the red line is the average of all six scans. **b)** 729 nm transition spectra in the presence of a 4 G magnetic field which splits the $S_{1/2}$ level into two levels (shown by the red and blue lines) and splits the $D_{3/2}$ transition into ten levels (eight of these are shown).

CHAPTER VII

CONCLUSION

Now that the Pulse Programmer can execute simple spectroscopy experiments, the immediate challenges are to experimentally realize sideband cooling and measure $D_{5/2}$ state populations for varying length 729 nm pulses (Rabi flopping). Demonstrating Rabi flopping proves that the Pulse Programmer can create arbitrary qubit transition pulses like the π and $\pi/2$ pulses perviously mentioned. After qubit transitions can be demonstrated for long coherence times, it will be possible to implement any arbitrary single-qubit gate. Another key progression for the Pulse Programmer will be the integration of new DAC modules. These new DAC modules will allow for greater micromotion compensation, allow for multiple trapping regions by giving improved DC voltage control, and allow ion shuttling experiments to be performed in the current Paul trap. If the new DACs prove successful and if Rabi coherence times can be extended far enough, it will eventually be possible to implement multiple-qubit gates with the Pulse Programmer.

APPENDIX A

RELATIONS BETWEEN A AND Q IN THE MATHIEU EQUATION TO THE SECOND ORDER

$$a_0 = -\frac{q^2}{2} + \frac{7q^4}{128} - \frac{29q^6}{2304} + \frac{68687q^8}{18874368} + O(q^{10}) \quad (65)$$

$$b_1 = 1 - q - \frac{q^2}{8} + \frac{q^3}{64} - \frac{q^4}{1536} + \frac{11q^5}{36864} + O(q^6) \quad (66)$$

$$a_1 = 1 + q - \frac{q^2}{8} - \frac{q^3}{64} - \frac{q^4}{1536} - \frac{11q^5}{36864} + O(q^6) \quad (67)$$

$$b_2 = 4 - \frac{q^2}{12} + \frac{5q^4}{13824} - \frac{289q^6}{79626240} + \frac{21391q^8}{458647124200} + O(q^{10}) \quad (68)$$

$$a_2 = 4 + \frac{5q^2}{12} - \frac{763q^4}{13824} + \frac{1002401q^6}{79626240} - \frac{1669086401q^8}{458647124200} + O(q^{10}) \quad (69)$$

REFERENCES

- [1] R. Blatt, and D. J. Wineland, *Nature*, **453**, 19 (2008)
- [2] R. Landauer, *IBM J. of Res. and Development* **5**, 3, (1961)
- [3] E. Fredkin, and T. Toffoli, *Int. J. of Theoretical Phys.* **21**, 3/4, (1981)
- [4] T. Toffoli, *Lecture Notes in Computer Sci.* **85**, (1980)
- [5] R. P. Feynman, *Foundations of Phys.*, **16**, 6, (1986)
- [6] A. Barenco *et al.*, *Phys. Rev. A* **52**, 5, (1995)
- [7] G. Vidal, and C. M. Dawson, *Phys. Rev. A* **69**, 1, (2004)
- [8] V. V. Shende, I. L. Markov, and S. S. Bullock, *Phys. Rev. A* **69**, 6, (2004)
- [9] J. I. Cirac, and P. Zoller, *Phys. Rev. Lett.* **74**, 20, (1995)
- [10] A. Sørensen, and K. Mølmer, *Phys. Rev. Lett.* **82**, 9, (1999)
- [11] B. Kraus, and J. I. Cirac, *Phys. Rev. A* **63**, 6, (2001)
- [12] J. P. Home *et al.*, *Science* **325**, 5945, (2009)
- [13] D. J. Wineland *et al.*, *J. Res. National Institute for Standards and Technology* **103**, (1998)
- [14] Q. A. Turchette *et al.*, *Phys. Rev. A* **81**, 2, (1998)
- [15] S. Olmschenk *et al.*, *Int. J. of Quantum Information* **8**, 1 & 2, (2010)
- [16] D. Hanneke *et al.*, *Nature Phys.* **6**, (2010)
- [17] J. T. Barreiro *et al.*, *Nature* **470**, (2011)
- [18] E. E. Edwards *et al.*, *Phys. Rev. B* **82**, 6, (2010)
- [19] T. Monz *et al.*, *Phys. Rev. Lett.* **106**, 13, (2011)
- [20] W. Paul, *Rev. of Modern Phys.* **62**, 3, (1990)
- [21] C. W. Chou *et al.*, *Phys. Rev. Lett.* **104**, 7, (2010)
- [22] C. R. Clark, *Phys. Rev. A* **81**, 4, (2010)
- [23] K. Chen *et al.*, *Phys. Rev. A* **83**, 3, (2011)

- [24] D. J. Griffiths, *Introduction to Electrodynamics* (Pearson Education, Upper Saddle River, NJ 1999)
- [25] R. E. March, *J. of Mass Spectrometry* **32**, (1997)
- [26] N. W. McLachlan, *Theory and Application of Mathieu Functions* (Oxford University Press, London, UK, 1947)
- [27] D. J. Berkeland *et al.*, *J. of Applied Phys.*, **83**, 10, (1998)
- [28] D. M. Lucas *et al.*, *Phys. Rev. A*, **69**, 1 (2004)
- [29] N. A. Gershenfeld, and I. L. Chuang, *Science*, **275**, 5298, (1997)
- [30] C. F. Roos, Karl-Franzens-Univ. Graz, (2000)
- [31] H. J. Metcalf, and P. van der Straten, *Laser Cooling and Trapping* (Springer-Verlag New York Inc., New York, NY 1999)
- [32] J. H. Wessenberg, *et al.*, *Phys. Rev. A*, **76**, 5 (2008)
- [33] M. A. Nielsen, and I. L. Chuang, *Quantum Computation and Quantum Information* (Cambridge University Press, Cambridge, UK, 2000).
- [34] D. J. Griffiths, *Introduction to Quantum Mechanics* (Pearson Education, Upper Saddle River, NJ 2005)
- [35] D. A. Steck, *Classical and Modern Optics* , available online at <http://steck.us/teaching> (revision 1.4.3, 21 December 2008)
- [36] Analog Devices, *A Technical Tutorial on Digital Synthesizers* (Analog Devices, Norwood, MA 1999)
- [37] Analog Devices, *AD9958 Manual* (Analog Devices, 2005)

An FPGA-Based Microarchitecture for the Implementation of Quantum Gates With Trapped Ions

C. Spencer Nichols

38 Pages

Directed by Professor Kenneth Brown

Quantum computing promises to revolutionize computing by providing exponential speed improvements to classically difficult problems. Over the past 30 years, experimental research has progressed from manipulating quantum systems to creating elementary gates in many quantum mechanical systems. One of the most successful media for implementing quantum gates is trapped ions. Current trapped-ion quantum computing architectures have very high gate fidelities and long coherence times, but creating quantum gates with low error rates with trapped ions is challenging since it requires precise trap and laser control. In order to implement quantum gates with trapped ions, I have created a field-programmable-gate-array- (FPGA) based microarchitecture for constructing laser-pulse sequences and controlling ancillary equipment. The microarchitecture is centralized to minimize experimental timing errors and is programmable to provide the generality necessary for implementing a vast range of experiments.